

The Close AGN Reference Survey (CARS): Dense and molecular gas tracers around AGN

Jacob S. Elford,^{1*} Timothy A. Davis,¹ Ilaria Ruffa¹ and Others²

¹Cardiff Hub for Astrophysics Research & Technology, School of Physics & Astronomy, Cardiff University, Queens Buildings, The Parade, Cardiff, CF24 3AA, UK

Accepted XXX. Received YYY; in original form ZZZ

ABSTRACT

Need to write

Key words: galaxies: active – galaxies: ISM – galaxies: nuclei

1 INTRODUCTION

Supermassive black holes (SMBH) are found in the centres of almost all massive galaxies ($M_* \gtrsim 10^9 M_\odot$). There are strong correlations between the mass of the SMBH and the properties of the host galaxies such as bulge mass: (e.g. Magorrian et al. 1998; Marconi & Hunt 2003) and velocity dispersion: (e.g. Ferrarese & Merritt 2000; Tremaine et al. 2002; Gültekin et al. 2009), which suggests a self regulated co-evolution between them (see e.g. Kormendy & Ho 2013 for a review). SMBH that are actively accreting material and feeding energy back into the host galaxies are commonly called Active Galactic Nuclei (AGN). There is a tight connection between the AGN and the surrounding interstellar medium (ISM) as the ISM could play a key role in fuelling AGN. On the other hand, there is evidence that the energetic output from AGN can change the physical conditions of the surrounding ISM and/or expel from the nuclear regions potentially explaining the SMBH-host galaxy co-evolution (e.g. Bower et al. 2006; Croton et al. 2006; King & Pounds 2015; Morganti 2017; Harrison 2017).

Using current mm-interferometers such as the Atacama Large Millimeter/submillimeter Array (ALMA) the cold molecular gas in galaxies has been studied using a variety of different tracer molecules including CO, HCN, HCO^+ and CS. CO is the typical molecule chosen to trace the cold molecular gas in the ISM of galaxies with the critical density of CO (1-0) transition being $\sim 1000 \text{ cm}^{-3}$. A number of studies have detected CO in the nuclear regions of AGN hosting galaxies using different CO transitions (e.g. García-Burillo et al. 2014; Moser et al. 2016; Koss et al. 2021; Lelli et al. 2022). HCN, HCO^+ and CS are typically used to trace dense molecular gas in the ISM as they have critical density of $\sim 10^4 \text{ cm}^{-3}$. Gao & Solomon (2004b,a) studied the HCN (1-0) line in a large survey of nearby spirals and (U)LIRGs and found a tight correlation between the infrared (IR) luminosity, indicative of star formation, and the HCN luminosity for normal star-forming and starburst galaxies. This implies that the dense molecular gas is the fuel for star formation rather than the total molecular gas. Tan et al. (2018) found similar correlations between the IR luminosity and both the HCN (4-3) transition and the HCO^+ (4-3) transition. These dense gas tracers have

been detected in AGN hosting galaxies (e.g. Baan et al. 2008; Krips et al. 2008; Juneau et al. 2009; García-Burillo et al. 2014; Moser et al. 2016; Li et al. 2021).

Many of these molecules have the potential to be used as useful observational tools to help classify AGN. A high intensity of HCN(1-0) with respect to $\text{HCO}^+(1-0)$ and/or CO(1-0) has been proposed as a feature unique to AGN (e.g. Jackson et al. 1993; Sternberg et al. 1994; Tacconi et al. 1994; Kohno et al. 2001; Usero et al. 2004; Kohno 2005; Imanishi et al. 2007; Krips et al. 2008; Davies et al. 2012). Izumi et al. (2013) found that in AGN the $\text{HCN}(4-3)/\text{HCO}^+(4-3)$ and $\text{HCN}(4-3)/\text{CS}(7-6)$ integrated intensity ratios seem to be higher than those in starburst galaxies. They then proposed a diagnostic diagram termed a "*submm-HCN diagram*" using these line ratios which was then expanded in Izumi et al. (2016).

However, more work need to be done to test how the results from this *submm-HCN diagram* compare to other methods of studying ionisation from AGN (e.g. in the optical with a BPT diagram Baldwin et al. (1981)). Additionally, more work needs to be done to fully understand the connection between AGN and the dense gas in their host galaxy.

The Close AGN Reference Survey (CARS, Husemann et al. 2017, 2019) is utilising facilities such as ALMA and the multi-unit spectroscopic explorer (MUSE, Bacon et al. (2010, 2014)) to study the most luminous type 1 AGN at redshifts $0.01 < z < 0.06$. In this paper, we use CARS observations of CO, HCN, HCO^+ and CS to map molecular and dense gas around 5 AGN from the CARS sample. We then produce the *submm-HCN diagram* for these objects to and compare the classification in the submm to the classification from methods using optical data to see if the ionisation mechanisms are the same at different wavelengths.

This paper is organised as follows. In Section 2, we describe the sample and the observations used for our analysis. We describe the methodology in Section 3. We present our results in Section 4 and discuss them in Section 5, before summarising and concluding in Section 6.

* E-mail: elfordj@cardiff.ac.uk

2 OBSERVATIONS

In this study we use both interferometric data from ALMA and IFU data from MUSE obtained as part of CARS. The CARS target are drawn from the Hamburg-ESO Survey (HES, [Wisotzki et al. 2000](#)), which is a purely flux-limited AGN catalog based on *B*-band photometry and slitless spectroscopy. A random sub-sample of these AGN in the redshift range $0.01 < z < 0.06$ have then been observed using the CO(1-0) line which defines the CARS targets ([Bertram et al. 2007](#); [König et al. 2009](#)).

2.1 ALMA

2.2 Line Imaging

From the CARS sample 5 galaxies were chosen to be observed in band 7 with ALMA via the HCN(4-3), HCO⁺(4-3) and the CS(7-6) lines to study the dense gas in these galaxies. The galaxies chosen were HE0108-4743, HE0433-1028, HE1029-1831, HE1108-2813 and HE1353-1917 and the observations were taken in 2018 (Project Code: 2017.1.00258.S). The spectral configuration of these observations consisted of 4 spectral windows (SPWs), three centred on the redshifted frequency of the three lines we wanted to observe (354.5 GHz for the HCN (4-3) line, 356.7 GHz for the HCO⁺ (4-3) line and 342.9 GHz for the CS (7-6) line). The final SPW was used to observe the continuum. HE0433-1028, HE1108-2813 and HE1353-1917 have also been ALMA band 3 observations of the CO(1-0) and ¹³CO(1-0) line with ALMA in 2016 (Project Code: 2016.1.00952.S). The spectral configuration of these observations consisted of 4 spectral windows (SPWs), 2 centred on the redshifted frequency of the 2 lines we wanted to observe (115.3 GHz for the CO (1-0) line and 110.2 GHz for the ¹³CO (1-0) line). The final 2 SPWs was used to observe the continuum. For both of these observing runs a standard calibration strategy was adopted for every observation. A single bright object (typically a quasar) was used as both flux and bandpass calibrator, while a second bright object was used as a phase calibrator.

All data sets were calibrated, combined and imaged using the ALMA pipeline, as provided by the European ALMA Regional Centre staff, and Common Astronomy Software Applications (CASA) package ([McMullin et al. 2007](#)). Continuum emission was measured over the full line-free bandwidth and was subtracted from the data in the *uv*-plane using the CASA task *uvcontsub*. The line data was then cleaned and imaged using the CASA task *tclean* and Briggs weighting of 0.5 to get the best trade-off between sensitivity and angular resolution. The angular resolution of each object is indicated in Table 1. The resulting 3D (RA, Dec, velocity) data cubes were produced with channel widths of 10 km s⁻¹ and a pixel size which approximately Nyquist sample the synthesised beam. The HCN data cubes had noises ranging from 0.466–1.26 mJy beam⁻¹, the HCO⁺ data cubes had noises ranging 0.499–1.38 mJy beam⁻¹, the CS data cubes have noises ranging from 0.547–1.43 mJy beam⁻¹, the CO data cubes have noises ranging from 0.374–0.895 mJy beam⁻¹ and the ¹³CO data cubes have noises ranging from 0.351–0.744 mJy beam⁻¹.

2.2.1 Continuum imaging

For each object, we produced continuum images using both the dense gas observations and CO observations where available. For SPWs centred on line emission, the line channels were identified and excluded. Then using the CASA task *TCLEAN* task in multi-frequency synthesis (mfs) the continuum images were made. We again used

Briggs weighting with a robust parameter of 0.5 allowing us to obtain a good trade-off between sensitivity and resolution. This resulted in synthesised beam sizes ranging from 0".704–0".863 (with physical scales ranging from 373–633 pc) for the dense gas frequency continuum maps and synthesised beam sizes ranging from 0".447–0".587 (with physical scales ranging from 284–426 pc) for the CO continuum maps. The final 1 σ root mean square (rms) noise levels range from 45.2–560 μ Jy beam⁻¹ for the dense gas frequency continuum maps, and from 11.4–20.8 μ Jy beam⁻¹ for the CO continuum maps. The continuum emission in both the dense frequency and CO frequency continuum images are unresolved. However, in the dense gas frequency continuum map of HE0433-1028 there appears to be 2 continuum sources that are not present in the CO continuum image. The continuum fluxes and the associated errors are presented in Table 1.

Look into spectral index using LSB and USB images. Look into the double continuum source.

2.3 MUSE

IFU observations for these 5 galaxies was obtained with the MUSE instrument at the Very Large Telescope ([Bacon et al. 2010, 2014](#)) under programs 094.B-0345(A) (HE0108-4743, HE0433-1028, HE1029-1831 and HE1108-2812) and 095.B-0015(A) (HE1353-1917). We refer the readers to [Husemann et al. \(2022\)](#) for the full details of the IFU observations and data reduction.

May need to expand on

3 METHODS

3.1 Stacking methodology

To improve detections of the HCN(4-3), HCO⁺(4-3), CS(7-6) and ¹³CO(1-0) lines we stacked this data with the CO(1-0) moment 1 maps where available and the MUSE moment 1 maps otherwise. The stacking spectra is as follows. Using the moment maps for each pixel in the data cube the velocity centre is determined. Then the spectra for each pixel is extracted and then the spectrum is adjusted so that its velocity centre aligns with a common velocity reference. These adjusted spectra are then added to create a stacked spectra which should enhance the detections of the lines observed. To measure the integrated intensities for the HCN(4-3), HCO⁺(4-3) and the CS(7-6) lines we fitted Gaussian to the stacked spectra using the Markov chain Monte Carlo (MCMC) code *GAStimator*¹.

Talk more about stacking procedure

3.2 ALMA data products

Integrated intensity (moment 0), mean line-of-sight velocity (moment 1) and observed velocity dispersion (moment 2) maps of the HCN, HCO⁺, CS and CO detections. To create these moment maps the cleaned continuum subtracted data cubes were used using the masked moment technique ([Dame 2011](#)). In this technique, a copy of the cleaned data cube is first Gaussian-smoothed spatially with a FWHM equal to 1.5 times that of the synthesised beam and then Hanning-smoothed in the velocity dimension. A three-dimensional mask is then created by selecting all the pixels above a fixed flux-density threshold. The moment maps were then constructed using the

¹ <https://github.com/TimothyADavis/GAStimator>

Table 1. Basic parameters of our galaxy sample.

Galaxy	z	SFR ($M_{\odot} \text{ yr}^{-1}$)	$S_{\text{cont,dense}}$ (mJy)	$\Delta S_{\text{cont,dense}}$ (mJy)	$S_{\text{cont,CO}}$ (mJy)	$\Delta S_{\text{cont,CO}}$ (mJy)	Beam _{HCN} (arcsec)	Beam _{HCO+} (arcsec)	Beam _{CS} (arcsec)	Beam _{CO} (arcsec)	Beam _{¹³CO} (arcsec)
(1)	(2)	(3)	(4)	(5)	(6)	(7)	(8)	(9)	(10)	(11)	(12)
HE0108-4743	0.024	$4.3^{+0.2}_{-0.2}$	0.174	0.0534	-	-	0.731	0.727	0.759	-	-
HE0433-1028	0.036	$19.4^{+0.2}_{-0.2}$	0.768	0.122	0.172	0.0146	0.899	0.900	0.936	0.406	0.417
HE1029-1831	0.041	$27.1^{+0.8}_{-1.3}$	0.570	0.0700	-	-	0.735	0.735	0.763	-	-
HE1108-2813	0.024	$12.4^{+0.4}_{-0.4}$	0.920	0.560	0.117	0.0208	0.789	0.789	0.818	0.520	0.528
HE1353-1917	0.035	$2.8^{+0.1}_{-0.1}$	0.0948	0.0452	0.0451	0.0114	0.694	0.692	0.719	0.533	0.557

Notes: (1) galaxy name and its redshift in (2). (3) star formation rate with associated errors. (4) flux density from the dense gas frequency continuum maps with the uncertainty in (5). (6) flux density from the CO continuum maps with the uncertainty in (7). (8)-(12) beam size of the HCN, HCO+, CS, CO and ¹³CO observations.

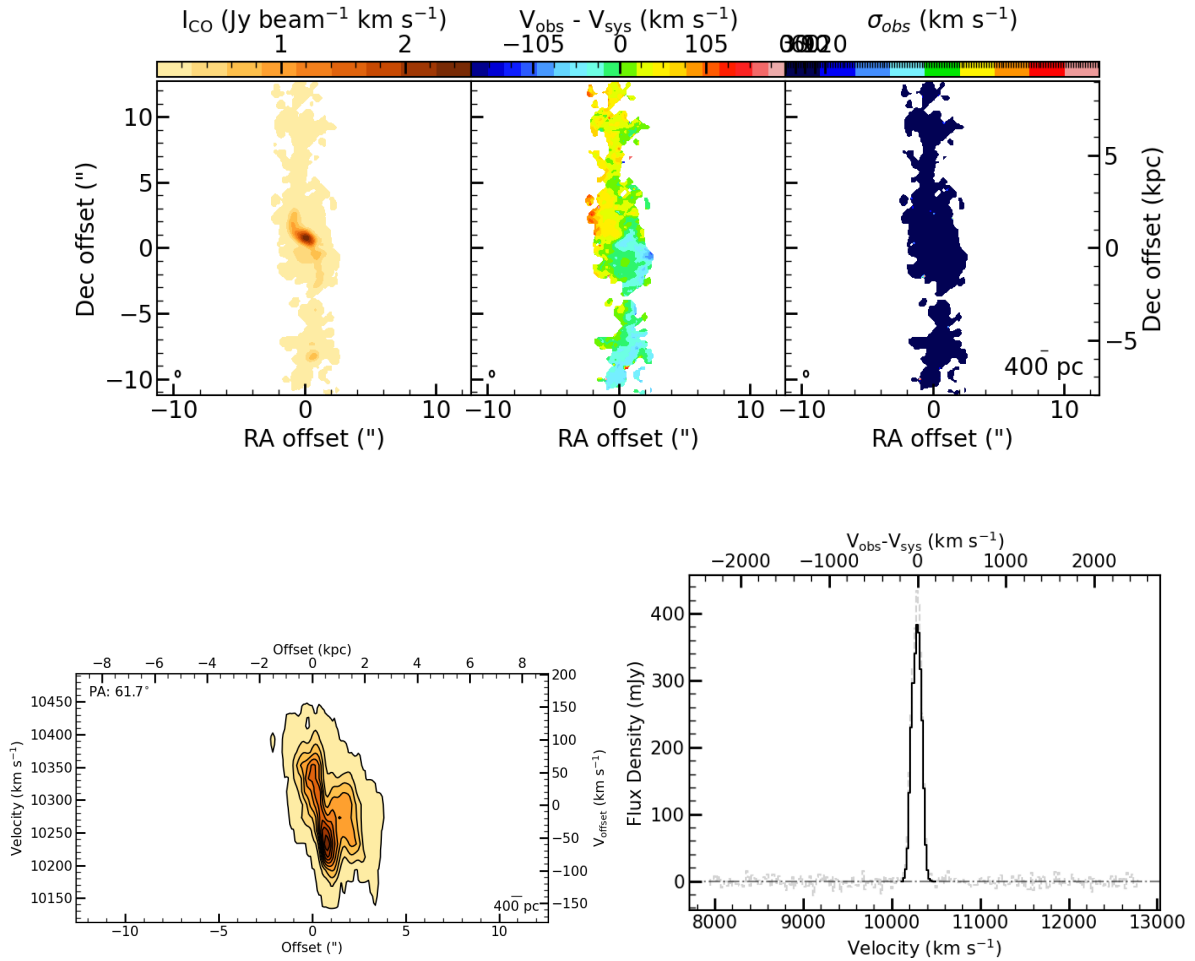


Figure 1. CO data products of the ALMA observations of HE0433-1028 with the moment map 0 (top left), moment 1 map (top middle) and moment 2 map (top right). The position velocity diagram is on the bottom left and the spectra is on the bottom right.

original un-smoothed cubes using the masked regions only. Major-axis position velocity diagrams (PVDs) were also constructed by summing the pixels in the masked cube within a pseudo-slit whose long axis is oriented with the position angle of the galaxy. Finally, the integrated spectrum was created by summing over both spatial dimensions in the data cube.

To produce these data products we utilise the code `pymakeplots`²

² <https://github.com/TimothyADavis/pymakeplots>

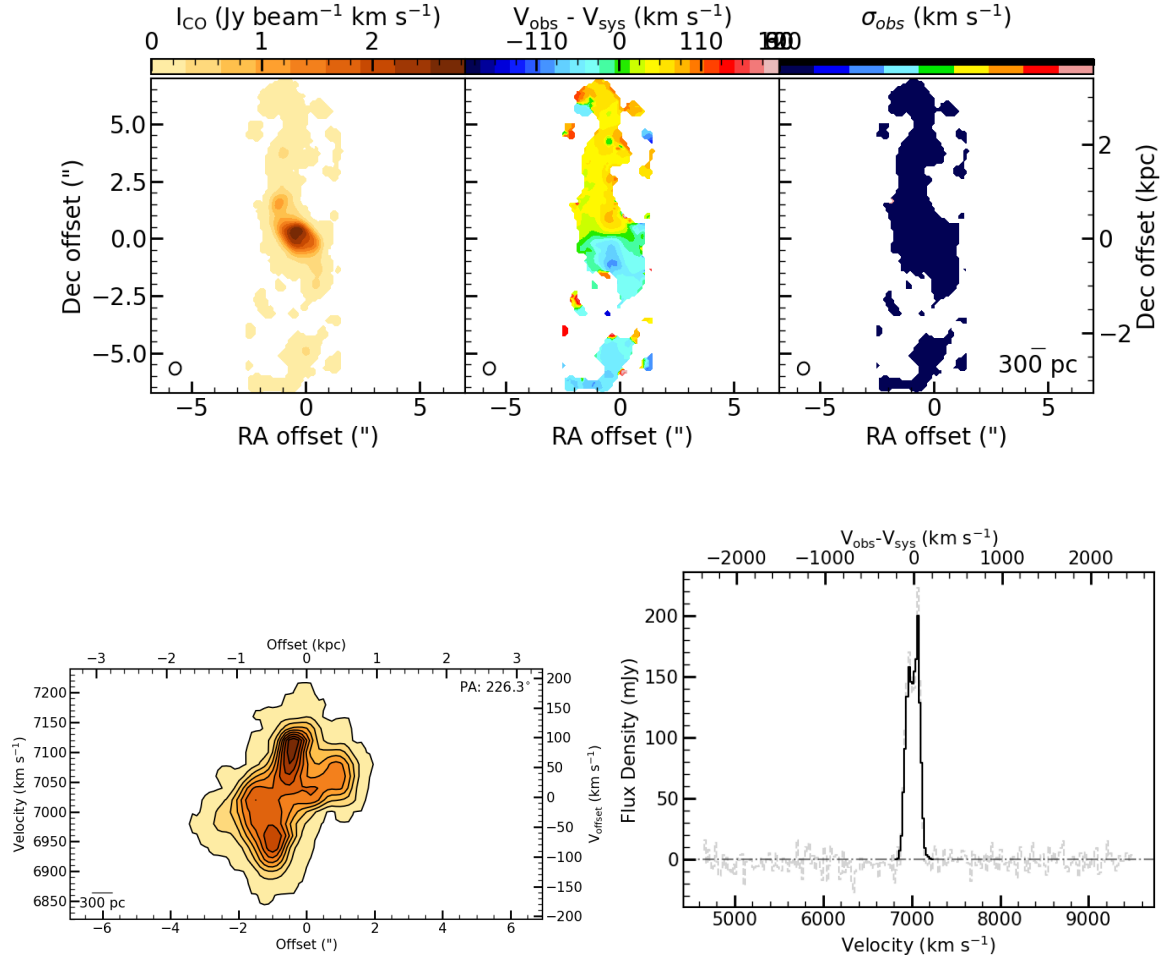


Figure 2. CO data products of the ALMA observations of HE1108-2813 with the moment map 0 (top left), moment 1 map (top middle) and moment 2 map (top right). The position velocity diagram is on the bottom left and the spectra is on the bottom right.

3.3 Optical AGN classification

To understand the dominant ionisation mechanisms in our 5 objects with use MUSE optical data to produce BPT, VO87-OI and VO87-SII diagrams for our objects.

In a BPT diagram (Baldwin et al. 1981) the $[\text{NII}]\lambda 6583/\text{H}\alpha$ and the $[\text{OIII}]\lambda 5007/\text{H}\beta$ ratios are used to classify objects as either star forming, composites, LINER or AGN dominated. We used the line from Kauffmann et al. (2003) to divide the pure star formation and composites regions

$$\log([\text{OIII}]/\text{H}\beta) = 0.61/(\log([\text{NII}]/\text{H}\alpha) - 0.05) + 1.3. \quad (1)$$

We used the line from Kewley et al. (2001) to separate the composite and the AGN/LINER regions

$$\log([\text{OIII}]/\text{H}\beta) = 0.61/(\log([\text{NII}]/\text{H}\alpha) - 0.47) + 1.19. \quad (2)$$

Finally, we used the line from Schawinski et al. (2007) to separate the AGN and LINER regions

$$\log([\text{OIII}]/\text{H}\beta) = 1.05\log([\text{NII}]/\text{H}\alpha) + 0.45. \quad (3)$$

In a VO87-OI diagram (Veilleux & Osterbrock 1987) the $[\text{OI}]\lambda 6300/\text{H}\alpha$ and $[\text{OIII}]\lambda 5007/\text{H}\beta$ ratios are used to classify objects as either star forming, LINER or Seyfert dominated. We used

the lines defined in Kewley et al. (2006) to separate the star forming, LINER and Seyfert dominated regions. The line that separates the star forming from the Seyfert/LINER dominated region is

$$\log([\text{OIII}]/\text{H}\beta) = 0.73/(\log([\text{OI}]/\text{H}\alpha) + 0.59) + 1.33 \quad (4)$$

and the line that separates the Seyfert from the LINER dominated region is

$$\log([\text{OIII}]/\text{H}\beta) = 1.18\log([\text{OI}]/\text{H}\alpha) + 1.30. \quad (5)$$

Similar to VO87-OI diagram a VO87-SII diagram (Veilleux & Osterbrock 1987) instead uses the $[\text{SII}]\lambda 67177/\text{H}\alpha$ ratio to classify objects as either star forming, LINER or Seyfert dominated. We again used the lines defined in Kewley et al. (2006) to separate the star forming, LINER and Seyfert dominated regions. The line that separates the star forming from the Seyfert/LINER dominated region is

$$\log([\text{OIII}]/\text{H}\beta) = 0.72/(\log([\text{SII}]/\text{H}\alpha) - 0.32) + 1.30 \quad (6)$$

and the line that separates the the Seyfert from the LINER dominated region is

$$\log([\text{OIII}]/\text{H}\beta) = 1.89\log([\text{SII}]/\text{H}\alpha) + 0.76. \quad (7)$$

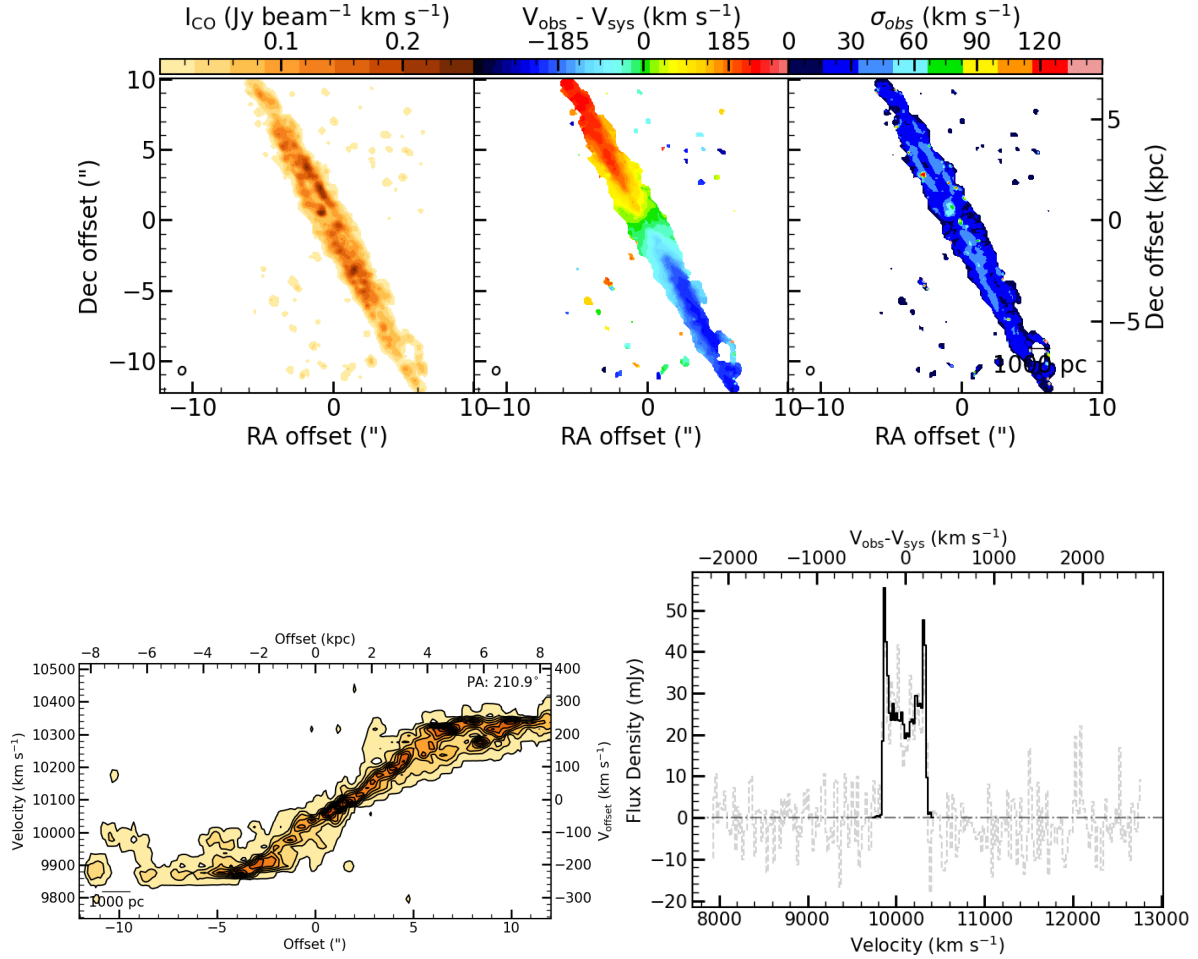


Figure 3. CO data products of the ALMA observations of HE1353-1917 with the moment map 0 (top left), moment 1 map (top middle) and moment 2 map (top right). The position velocity diagram is on the bottom left and the spectra is on the bottom right.

Using these definitions we produce global BPT, VO87-OI and VO87-SII diagrams for our 5 objects. In addition to the global diagrams we also produce these diagrams only including the nuclear points. The nuclear points are computed by taking the optical MUSE data only from within one ALMA beam used to observe the object.

4 RESULTS

4.1 ALMA Data

In Figures 1–3 we show the detections of CO in HE0433-1028, HE1108-2813 and HE1353-1917 respectively. The three observations of CO in these three objects are well resolved. The moment maps of HE1353-1917 (Figure 3) shows a regularly rotating CO disc. The moments maps of HE0433-1028 and HE1108-2813 (Figures 1 and 2) show more messy discs with more chaotic rotation. The PVD of HE1353-1917 shows the expected Keplerian rise which is not as clear in HE0433-1028 and HE1108-2813. The spectra of HE1353-1917 shows the typical double-horned shape of a rotating disc whilst the spectra of HE0433-1028 and HE1108-2813 have a Gaussian shape. We present the line intensities of the CO observations in Table 2.

In Figures A1–A3 we show the detections of HCN in HE0433-

1028, HE1029-1831 and HE1108-2813 respectively. HCN was not detected in HE0108-4743 or HE1353-1917.

In Figures A4–A6 we show the detections of HCO+ in HE0433-1028, HE1029-1831 and HE1108-2813 respectively. HCO+ was not detected in HE0108-1831 and HE1108-2813.

CS and $^{13}\text{CO}(1-0)$ was not detected in any of the sources. Looking at the data products of the HCN and HCO+ observation show that these observation were not very well resolved and thus the moment maps and position-velocity diagrams do not yield much information.

4.2 Stacked detections

We used the stacking procedure detailed in Section 3.1 to try and improve the detection of HCN, HCO+, CS and ^{13}CO we used the stacking procedure detailed in Section 3.1. In Figures 4–7 we present the HCN, HCO+, CS and ^{13}CO stacked spectra for our 5 objects. We still detect HCN in the 3 objects where it was detected pre-stacking but we still do not detect HCN in the other 2 objects. Similarly, we still detect HCO+ in the 3 objects where it was detected previously but we still do not detect it in the other 2 objects. However, we do

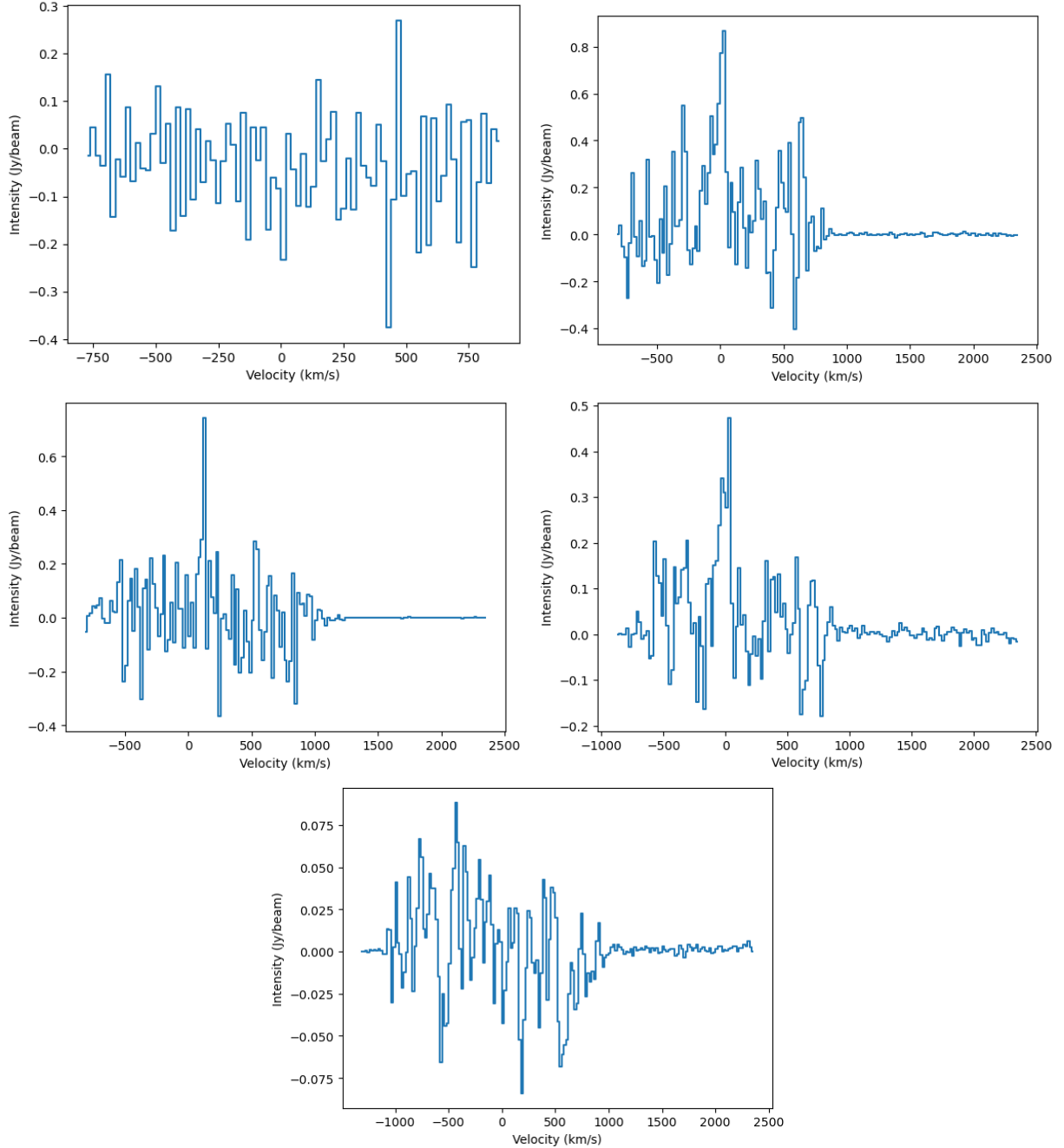


Figure 4. Stacked spectra of the HCN (4-3) line with HE0108-4743 (top left), HE0433-1028 (top right), HE1029-1831 (middle left), HE1108-2813 (middle right) and HE1353-1917 (bottom).

now detect CS in 1 of our objects (HE1108-2813) where we did not detect it previously. We still not detect it in the other 4 objects. Finally, we still do not detect ^{13}CO in the three objects where we aimed to observe it after stacking. In Table 2 we list the line intensities of the detected lines using a Gaussian fit for the undetected lines we instead present an upper limit as three times the RMS.

4.3 MUSE Data

In Figure 8 we present the global and nuclear BPT, VO87-OI and VO87-SII diagrams for HE0108-4743. The global and nuclear BPT,

VO87-OI and VO87-SII diagrams for HE0433-1028, HE1029-1931, HE1108-2813 and HE1353-1917 are shown in Figures A7-A10.

We find for one object (HE1353-1917) the nuclear BPT points lie exclusively in the AGN dominated region. Two of the objects (HE0108-4743 and HE0433-1028) have nuclear BPT points primarily in the AGN dominated regions with a few points in the composite and LINER regions respectively. One of the objects (HE1108-2813) has nuclear BPT points that fall in the composite, LINER and AGN regions. Finally, for one object (HE1029-1831) we find the nuclear BPT points lie exclusively in the composite region of the diagram.

In the VO87-OI diagrams we find two objects (HE0108-4743 and

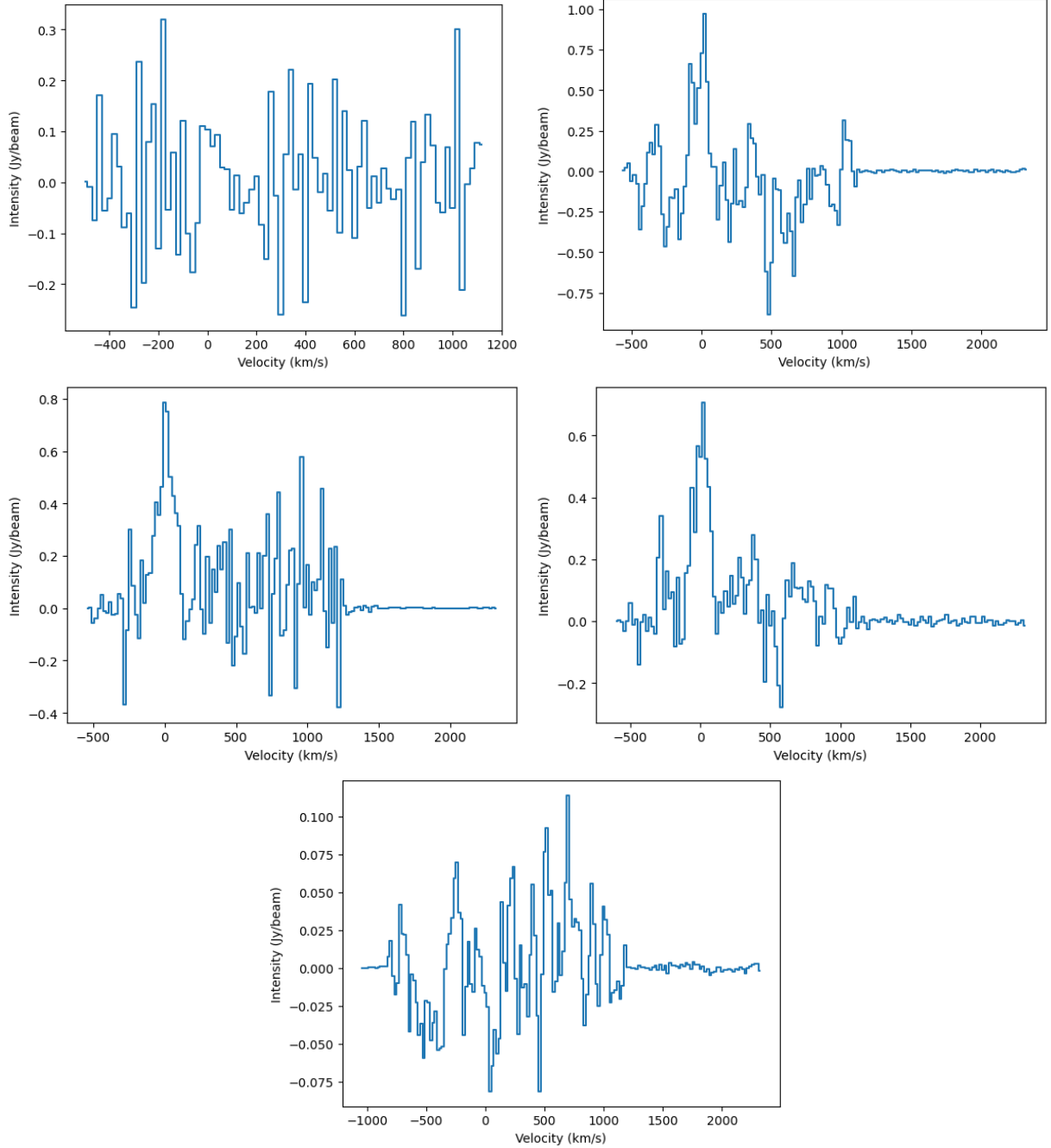


Figure 5. Stacked spectra of the HCO+ (4-3) line with HE0108-4743 (top left), HE0433-1028 (top right), HE1029-1831 (middle left), HE1108-2813 (middle right) and HE1353-1917 (bottom).

HE1029-1831) the nuclear points lie exclusively in the HII region. One object (HE1353-1917) has nuclear VO87-OI points primarily in the Seyfert region with a few points falling in the HII region of the diagram. One object (HE1108-2813) has nuclear VO87-OI points that fall primarily in the HII region with two points that fall in the Seyfert region. Finally, for one object (HE0433-1028) the nuclear VO87-OI lie roughly equally between the Seyfert and HII regions.

In the VO87-SII diagrams we find one object (HE1352-1917) with nuclear points exclusively in the Seyfert region. One object (HE1029-1831) has nuclear VO87-SII points exclusively in the HII region. One object (HE0108-4743) has nuclear VO87-SII points primarily in the

HII region with a few points in the Seyfert region. Finally, two objects (HE0433-1028 and HE1108-2813) have a number of nuclear points both in the Seyfert and the HII regions.

5 DISCUSSION

5.1 submm HCN diagram

To compare the optical classification classification to the classification we produce the submm-HCN diagram for our objects using the HCN(4-3)/CS(7-6) and HCN(4-3)/HCO+(4-3) ratios. As presented

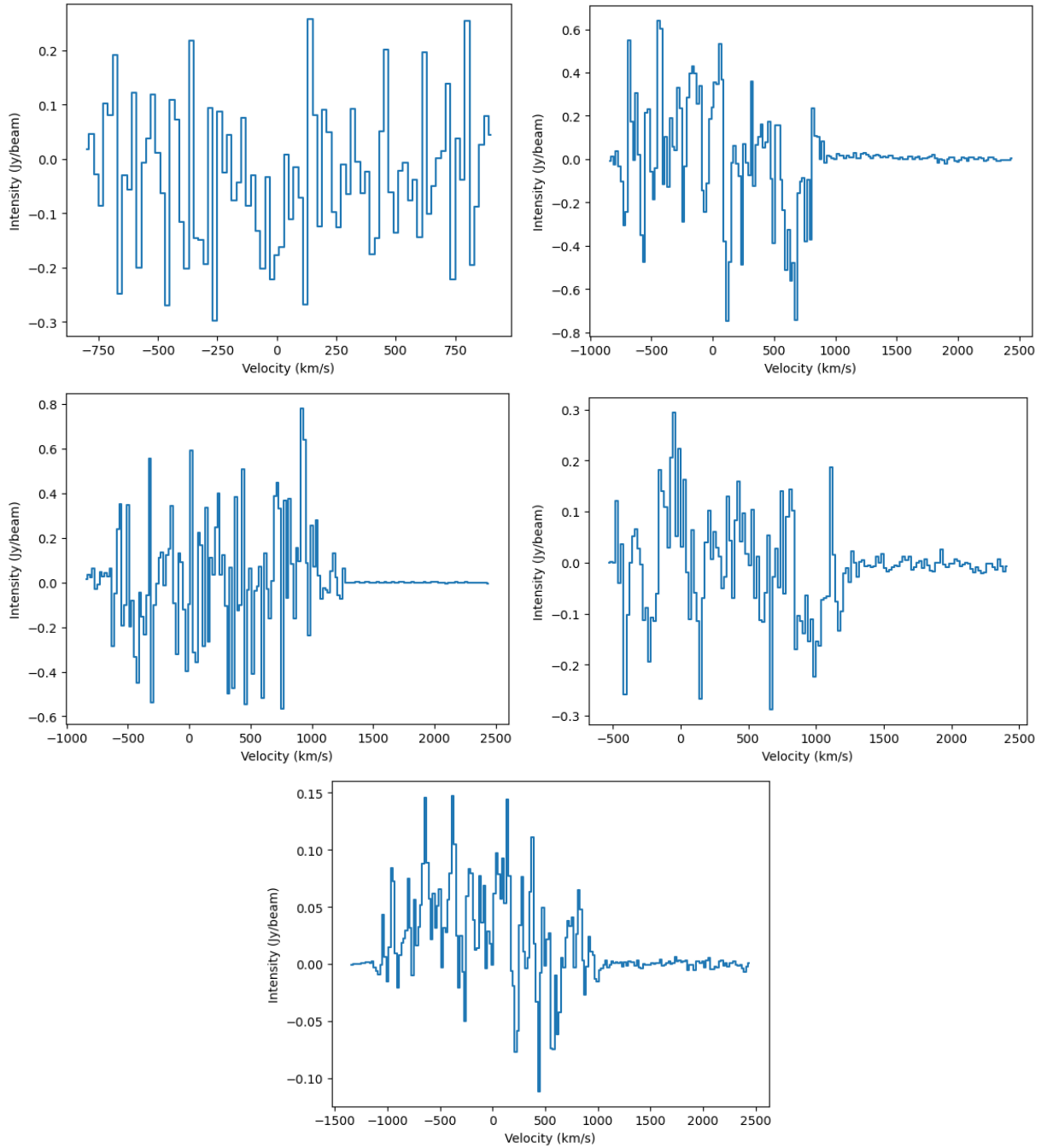


Figure 6. Stacked spectra of the CS (7-6) line with HE0108-4743 (top left), HE0433-1028 (top right), HE1029-1831 (middle left), HE1108-2813 (middle right) and HE1353-1917 (bottom).

in 4.1 we only detect these three lines in one of our objects, HE1108-2813. However, we have detections of HCN(4-3) and HCO+(4-3) in two other objects, HE0433-1028 and HE1029-1831, allowing us to use the non-detections of CS(7-6) in these objects to place lower limits on the HCN(4-3)/CS(7-6) ratio. Using this data we produce the submm-HCN diagram, shown in Figure 9, for our three objects. We additionally plot the points on this diagram from Izumi et al. (2016) and Zhang et al. (2014). We find that for the one object in which all three lines were detected, HE1108-2813, it lies in the starburst region of the submm-HCN diagram. The two objects where the CS(7-6) line was not detected, HE0433-2813 and HE1029-1831, the lower limits

also lie in the starburst region of the diagram though as these are lower limits these points could in reality lie in the AGN region of the diagram. All three points of our points lying in the starburst region of the sub-mm diagram is surprising as these objects are all luminous type 1 AGN so would be expected to lie in the AGN region of the diagram.

In Table 3 we list the different classifications for our objects. HE1353-1917 was the only object with consistent classification with it being classified as an AGN in all three optical classification methods. We were unable to classify this object using the submm-HCN diagram as the lines required were not detected. The BPT classifica-

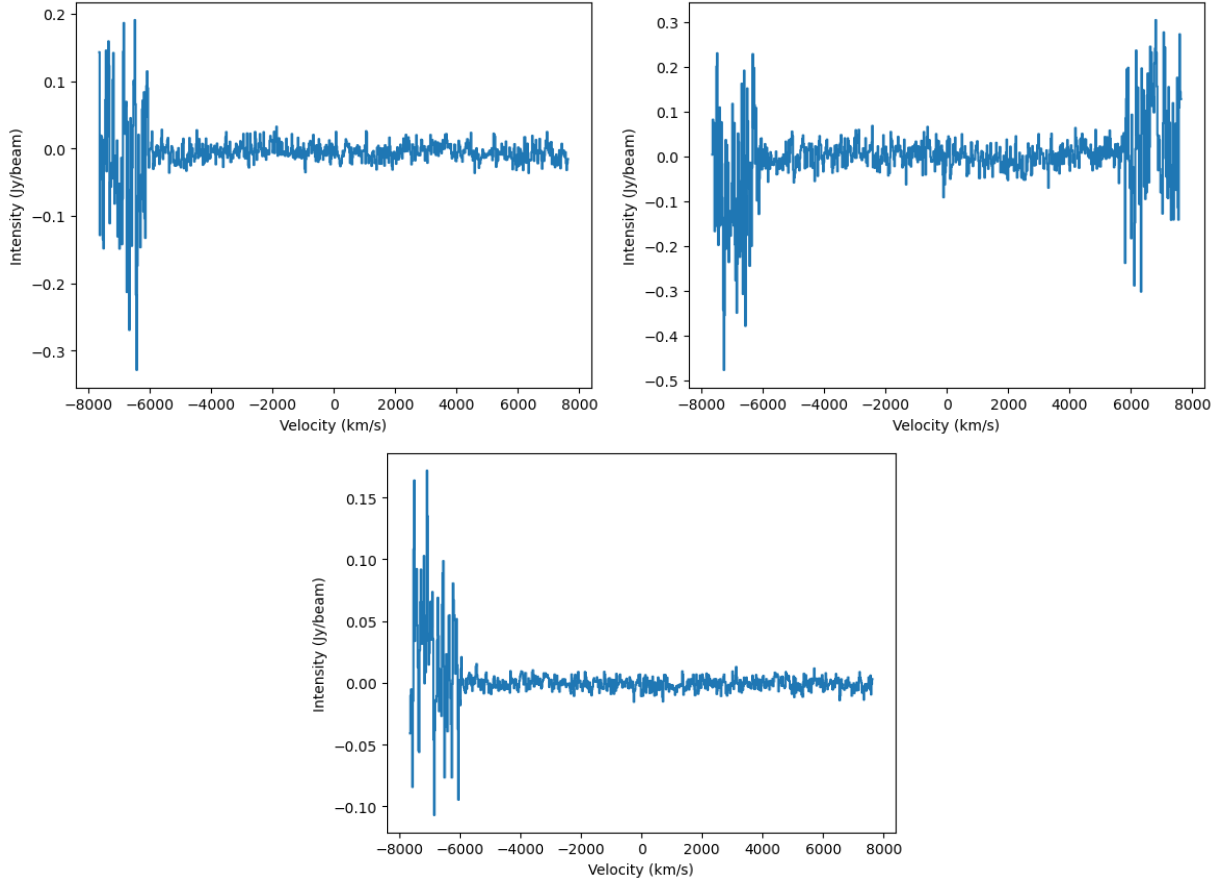


Figure 7. Stacked spectra of the ^{13}CO (1-0) line with HE0433-1028 (top left), HE1108-2813 (top right) and HE1353-1917 (bottom).

Table 2. Line Intensities after stacking

Galaxy	$I_{\text{HCN}(4-3)}$ (Jy km s $^{-1}$)	$I_{\text{HCO}^+(4-3)}$ (Jy km s $^{-1}$)	$I_{\text{CS}(7-6)}$ (Jy km s $^{-1}$)	$I_{\text{CO}(1-0)}$ (Jy km s $^{-1}$)	$I_{\text{CO}^{13}(1-0)}$ (Jy km s $^{-1}$)
(1)	(2)	(3)	(4)	(5)	(6)
HE0108-4743	<0.573	<0.629	<0.482	-	-
HE0433-1028	2.25 ± 0.11	2.39 ± 0.12	<1.08	51.9 ± 0.04	<0.443
HE1029-1831	0.600 ± 0.087	2.48 ± 0.16	<0.768	-	-
HE1108-2813	0.777 ± 0.064	1.53 ± 0.059	0.421 ± 0.059	30.6 ± 0.08	<0.581
HE1353-1917	<0.437	<0.473	<0.404	14.2 ± 0.04	<0.543

Notes: (1) galaxy name. (2)-(6) HCN (4-3), HCO $^+$ (4-3), CS (7-6), CO (1-0) and CO 13 (1-0) line intensity and associated uncertainties. All these lines except CO (1-0) are the line intensities after stacking.

tion was mostly consistent with all 5 of our objects being identified as having AGN contribution. HE1029-1831 was the only difference in the BPT classification as the object had no nuclear BPT points in the AGN region with the points exclusively lying in the composite region. The VO87-OI and VO87-SII classifications tend to agree with each other with both methods identifying star formation contribution and tend to disagree with the BPT classification with HE1353-1917 being the only exception. The submm-HCN diagram classification disagrees with the BPT classification with the submm-HCN diagram identifying the galaxies as star formation dominated whilst the BPT diagram mostly identify the galaxies as AGN dominated. On the other hand, the submm-HCN classification tends to agree with the VO87-OI and VO87-SII classification as they all identify star formation contribution. Further observations of the dense gas around AGN

is required to further populate the submm-HCN diagram and to fully understand why the classification from this method differs from the classification from other methods.

May need more detail. Why are classification schemes different?

5.2 Gao-Solomon relation

In Figure 10 we relate the HCN(4-3) and HCO $^+$ (4-3) luminosities with the infrared luminosities derived from the star formation rates. We do this to compare the dense gas detected in our objects with known star formation rate relations. We use the relations between the infrared luminosities and the HCN(4-3) and HCO $^+$ (4-3) luminosities from Tan et al. (2018) and additionally plot their points to compare with our results. To compute the infrared luminosities we use the

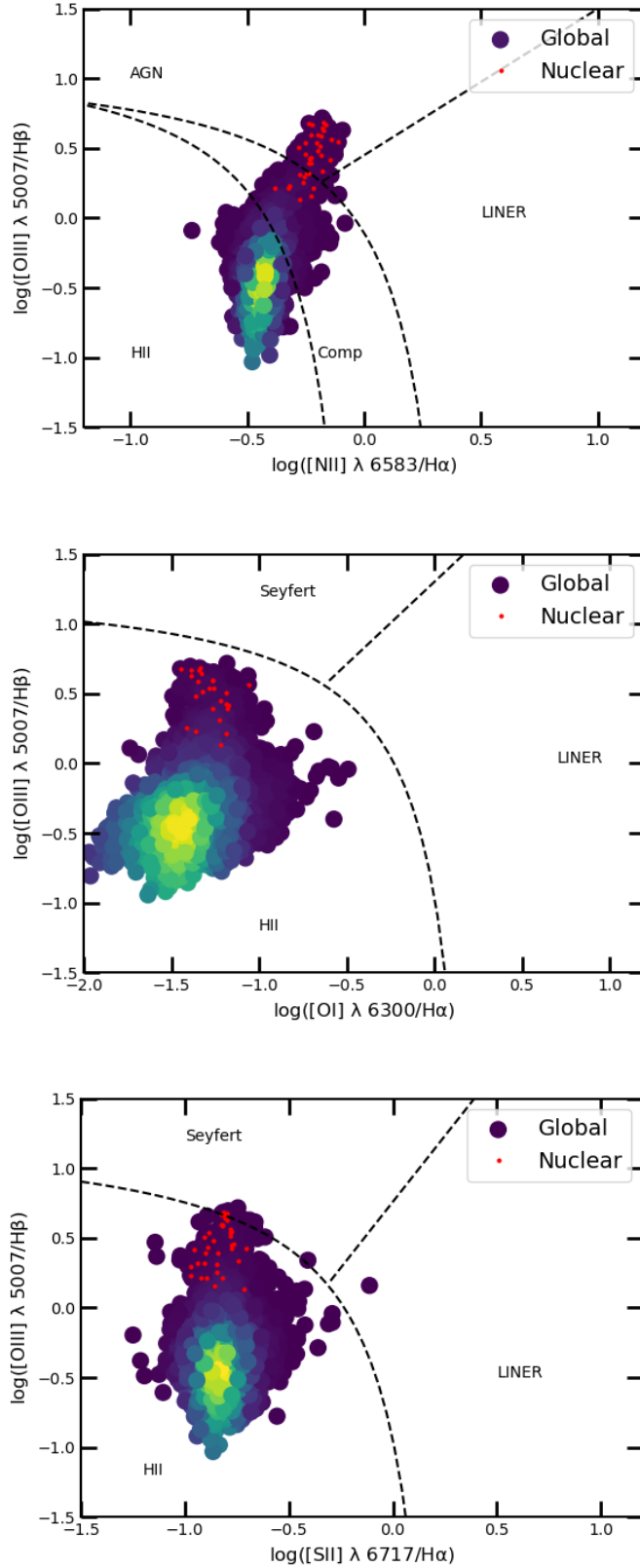


Figure 8. Global optical AGN classifications for HE0108-4743 with the BPT diagram at the top, the VO87-OI diagram in the middle and the VO87-SII diagram at the bottom. The red points represent the nuclear region taken within one ALMA beam size.

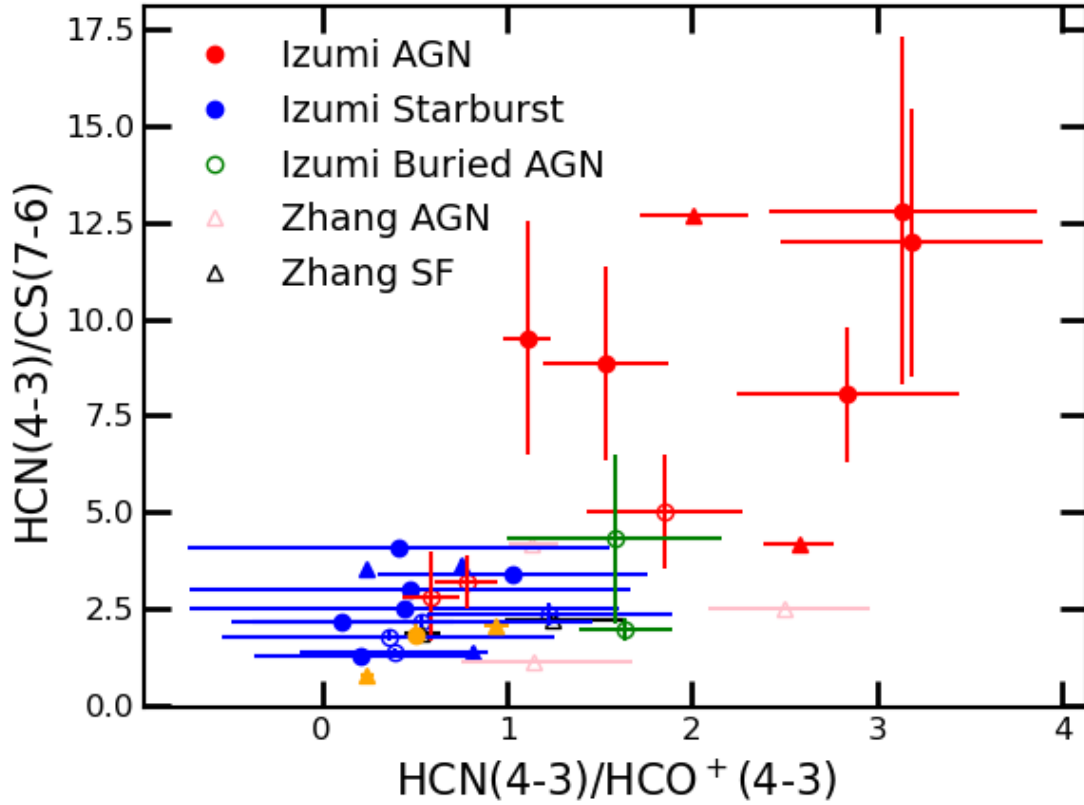


Figure 9. HCN diagram using the $\text{HCN}(4-3)/\text{HCO}^+(4-3)$ and the $\text{HCN}(4-3)/\text{CS}(7-6)$ ratios with the three galaxies from our sample where we have these ratios in yellow. We have also plotted the points from *Izumi et al. (2016)* and *Zhang et al. (2014)*. Triangles represent lower limits of these ratios and open symbols represent lower resolution observations.

Table 3. AGN classification comparison

Galaxy	BPT	VO87-OI	VO87-SII	submm-HCN
HE0108-4743	AGN/Comp	HII	HII	-
HE0433-1028	AGN	Seyfert/HII	Seyfert/HII	SB
HE1029-1831	Comp	HII	HII	SB
HE1108-2813	AGN/Comp	HII	Seyfert/HII	SB
HE1353-1917	AGN	Seyfert	Seyfert	-

relation between star formation rate and infrared luminosity as also used in *Gao & Solomon (2004b)*

$$\text{SFR} \approx 2 \times 10^{-10} (L_{\text{IR}}/L_{\odot}) \text{M}_{\odot} \text{yr}^{-1}. \quad (8)$$

The star formation rates of the our 5 CARS objects were taken from *Smirnova-Pinchukova et al. (2022)* and are listed in Table 1. We find that for both the HCN and HCO^+ luminosities for the three CARS source they appear to follow the same relation as found in *Tan et al. (2018)*. However, to fully understand the connection between the dense gas in galaxies and AGN further observations of dense gas in AGN hosting galaxies is required.

Need to look into nuclear star formation rates

6 CONCLUSIONS

Need to write

ACKNOWLEDGEMENTS

This work is supported by the UKRI AIMLAC CDT, funded by grant EP/S023992/1. TAD and IR acknowledges support from STFC grant ST/S00033X/1.

This research made use of *ASTROPY*³, a community-developed PYTHON package for Astronomy (*Astropy Collaboration et al.*

³ <http://www.astropy.org/>

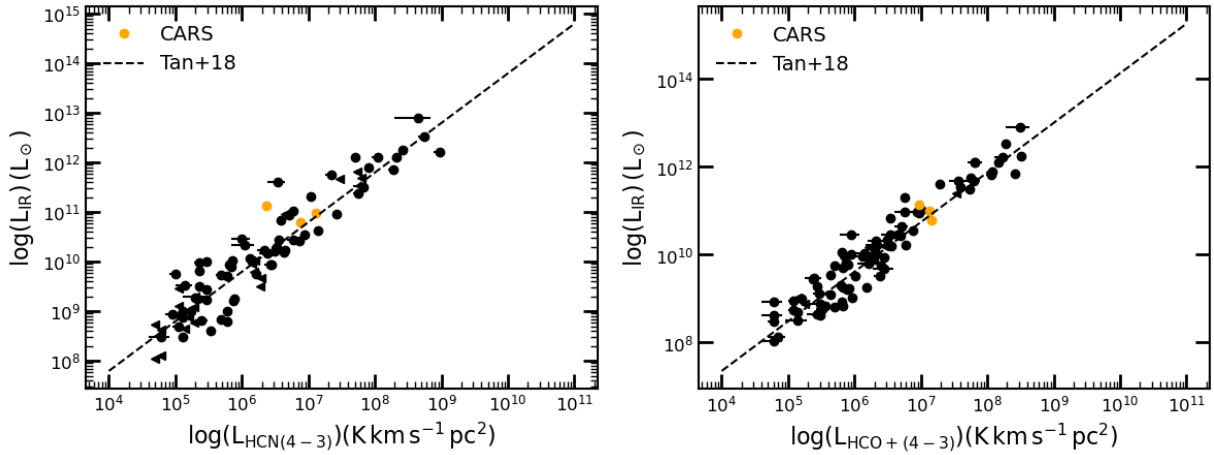


Figure 10. Relation between HCN(4-3) (left) and HCO+(4-3) (right) luminosity and the IR luminosity inferred from star formation. We additionally plot the points and relation from Tan et al. (2018).

2013), MATPLOTLIB⁴, an open source visualisation package (Hunter 2007) and NUMPY⁵, an open source numerical computation library (Harris et al. 2020)

This paper makes use of ALMA data. ALMA is a partnership of the ESO (representing its member states), NSF (USA), and NINS (Japan), together with the NRC (Canada), NSC, ASIAA (Taiwan), and KASI (Republic of Korea), in cooperation with the Republic of Chile. The Joint ALMA Observatory is operated by the ESO, AUI/NRAO, and NAOJ.

DATA AVAILABILITY

The data underlying this article are available in the ALMA archive, at <http://almascience.eso.org/aq/>. The data used and the final plots will be shared upon a reasonable request to the first author.

REFERENCES

- Astropy Collaboration et al., 2013, *A&A*, **558**, A33
- Baan W. A., Henkel C., Loenen A. F., Baudry A., Wiklind T., 2008, *A&A*, **477**, 747
- Bacon R., et al., 2010, in McLean I. S., Ramsay S. K., Takami H., eds, Society of Photo-Optical Instrumentation Engineers (SPIE) Conference Series Vol. 7735, Ground-based and Airborne Instrumentation for Astronomy III. p. 773508 ([arXiv:2211.16795](https://arxiv.org/abs/2211.16795)), doi:10.1117/12.856027
- Bacon R., et al., 2014, *The Messenger*, **157**, 13
- Baldwin J. A., Phillips M. M., Terlevich R., 1981, *PASP*, **93**, 5
- Bertram T., Eckart A., Fischer S., Zuther J., Straubmeier C., Wisotzki L., Krips M., 2007, *A&A*, **470**, 571
- Bower R. G., Benson A. J., Malbon R., Helly J. C., Frenk C. S., Baugh C. M., Cole S., Lacey C. G., 2006, *MNRAS*, **370**, 645
- Croton D. J., et al., 2006, *MNRAS*, **365**, 11
- Dame T. M., 2011, [arXiv e-prints](https://arxiv.org/abs/1101.1499), p. [arXiv:1101.1499](https://arxiv.org/abs/1101.1499)
- Davies R., Mark D., Sternberg A., 2012, *A&A*, **537**, A133
- Ferrarese L., Merritt D., 2000, *ApJ*, **539**, L9
- Gao Y., Solomon P. M., 2004a, *ApJS*, **152**, 63
- Gao Y., Solomon P. M., 2004b, *ApJ*, **606**, 271
- García-Burillo S., et al., 2014, *A&A*, **567**, A125
- Gültekin K., et al., 2009, *ApJ*, **698**, 198
- Harris C. R., et al., 2020, *Nature*, **585**, 357
- Harrison C. M., 2017, *Nature Astronomy*, **1**, 0165
- Hunter J. D., 2007, *Computing in Science and Engineering*, **9**, 90
- Husemann B., et al., 2017, *The Messenger*, **169**, 42
- Husemann B., et al., 2019, *A&A*, **627**, A53
- Husemann B., et al., 2022, *A&A*, **659**, A124
- Imanishi M., Nakanishi K., Tamura Y., Oi N., Kohno K., 2007, *AJ*, **134**, 2366
- Izumi T., et al., 2013, *PASJ*, **65**, 100
- Izumi T., et al., 2016, *ApJ*, **818**, 42
- Jackson J. M., Paglione T. A. D., Ishizuki S., Nguyen-Q-Rieu 1993, *ApJ*, **418**, L13
- Juneau S., Narayanan D. T., Moustakas J., Shirley Y. L., Bussmann R. S., Kennicutt R. C. J., Vanden Bout P. A., 2009, *ApJ*, **707**, 1217
- Kauffmann G., et al., 2003, *MNRAS*, **346**, 1055
- Kewley L. J., Dopita M. A., Sutherland R. S., Heisler C. A., Trevena J., 2001, *ApJ*, **556**, 121
- Kewley L. J., Groves B., Kauffmann G., Heckman T., 2006, *MNRAS*, **372**, 961
- King A., Pounds K., 2015, *ARA&A*, **53**, 115
- Kohno K., 2005, in Hüttmeister S., Manthey E., Bomans D., Weis K., eds, American Institute of Physics Conference Series Vol. 783, The Evolution of Starbursts. pp 203–208 ([arXiv:astro-ph/0508420](https://arxiv.org/abs/astro-ph/0508420)), doi:10.1063/1.2034987
- Kohno K., Matsushita S., Vila-Vilaró B., Okumura S. K., Shibatsuka T., Okiura M., Ishizuki S., Kawabe R., 2001, in Knapen J. H., Beckman J. E., Shlosman I., Mahoney T. J., eds, Astronomical Society of the Pacific Conference Series Vol. 249, The Central Kiloparsec of Starbursts and AGN: The La Palma Connection. p. 672 ([arXiv:astro-ph/0206398](https://arxiv.org/abs/astro-ph/0206398)), doi:10.48550/arXiv.astro-ph/0206398
- König S., Eckart A., García-Marín M., Huchtmeier W. K., 2009, *A&A*, **507**, 757
- Kormendy J., Ho L. C., 2013, *ARA&A*, **51**, 511
- Koss M. J., et al., 2021, *ApJS*, **252**, 29
- Krips M., Neri R., García-Burillo S., Martín S., Combes F., Graciá-Carpio J., Eckart A., 2008, *ApJ*, **677**, 262
- Lelli F., Davis T. A., Bureau M., Cappellari M., Liu L., Ruffa I., Smith M. D., Williams T. G., 2022, *MNRAS*, **516**, 4066
- Li F., et al., 2021, *MNRAS*, **503**, 4508
- Magorrian J., et al., 1998, *AJ*, **115**, 2285
- Marconi A., Hunt L. K., 2003, *ApJ*, **589**, L21
- McMullin J. P., Waters B., Schiebel D., Young W., Golap K., 2007, in Shaw R. A., Hill F., Bell D. J., eds, Astronomical Society of the Pacific Conference Series Vol. 376, Astronomical Data Analysis Software and Systems XVI. p. 127

⁴ <https://matplotlib.org/>

⁵ <https://numpy.org/>

- Morganti R., 2017, *Frontiers in Astronomy and Space Sciences*, 4, 42
- Moser L., et al., 2016, *A&A*, 587, A137
- Schawinski K., Thomas D., Sarzi M., Maraston C., Kaviraj S., Joo S.-J., Yi S. K., Silk J., 2007, *MNRAS*, 382, 1415
- Smirnova-Pinchukova I., et al., 2022, *A&A*, 659, A125
- Sternberg A., Genzel R., Tacconi L., 1994, *ApJ*, 436, L131
- Tacconi L. J., Genzel R., Blietz M., Cameron M., Harris A. I., Madden S., 1994, *ApJ*, 426, L77
- Tan Q.-H., et al., 2018, *ApJ*, 860, 165
- Tremaine S., et al., 2002, *ApJ*, 574, 740
- Usero A., García-Burillo S., Fuente A., Martín-Pintado J., Rodríguez-Fernández N. J., 2004, *A&A*, 419, 897
- Veilleux S., Osterbrock D. E., 1987, *ApJS*, 63, 295
- Wisotzki L., Christlieb N., Bade N., Beckmann V., Köhler T., Vanelle C., Reimers D., 2000, *A&A*, 358, 77
- Zhang Z.-Y., Gao Y., Henkel C., Zhao Y., Wang J., Menten K. M., Güsten R., 2014, *ApJ*, 784, L31

APPENDIX A: OTHER PLOTS

This paper has been typeset from a \LaTeX file prepared by the author.

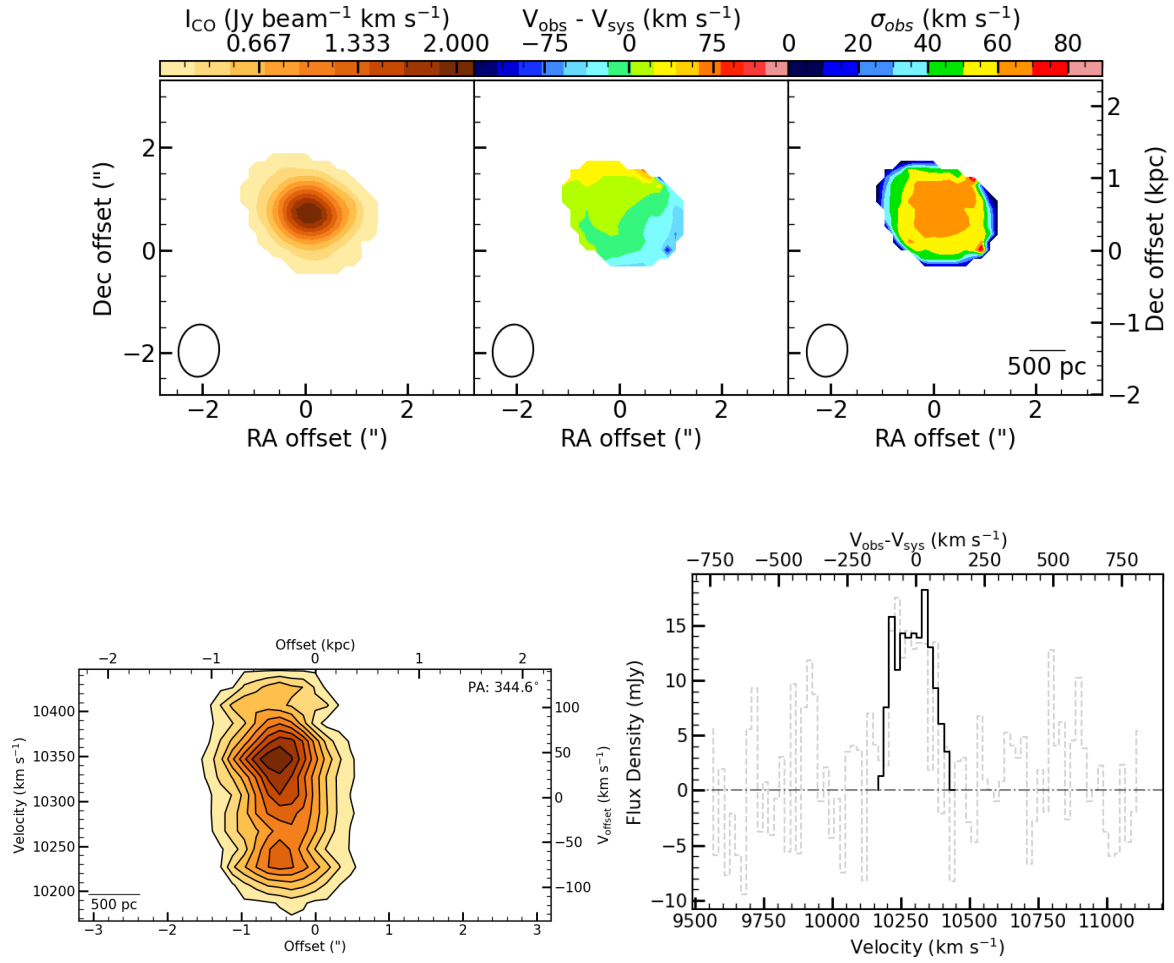


Figure A1. HCN data products of the ALMA observations of HE0433-1028 with the moment map 0 (top left), moment 1 map (top middle) and moment 2 map (top right). The position velocity diagram is on the bottom left and the spectra is on the bottom right.

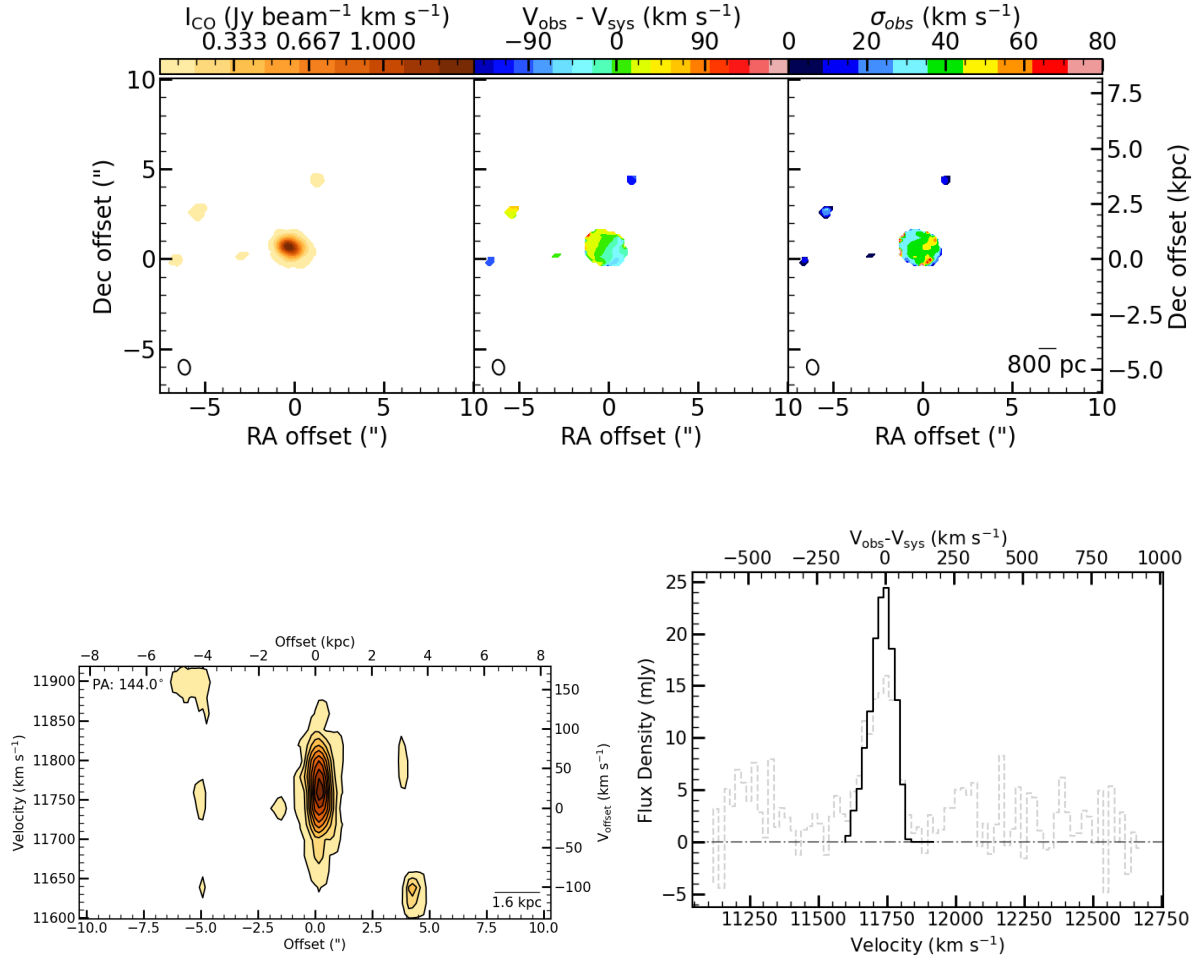


Figure A2. HCN data products of the ALMA observations of HE1029-1831 with the moment map 0 (top left), moment 1 map (top middle) and moment 2 map (top right). The position velocity diagram is on the bottom left and the spectra is on the bottom right.

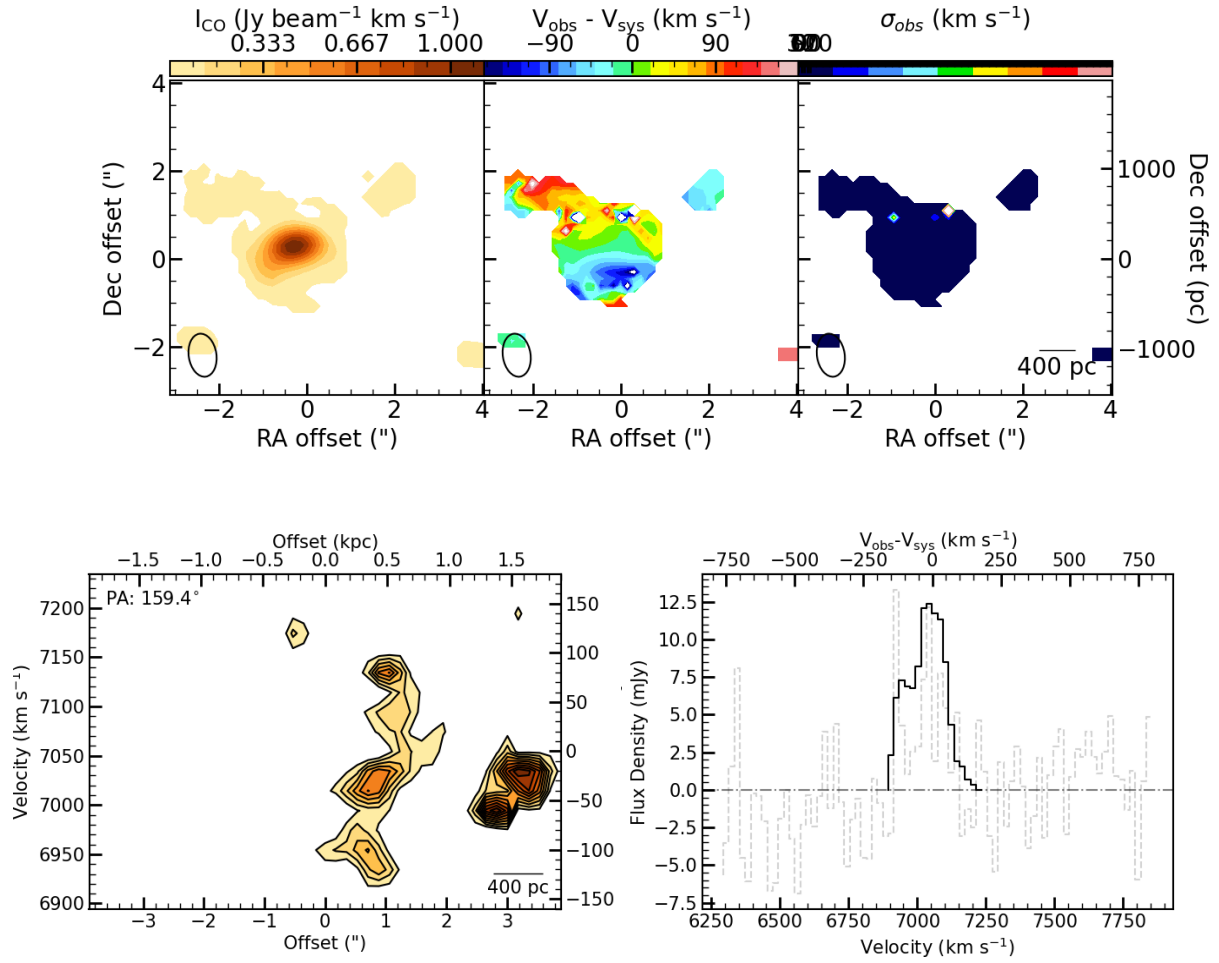


Figure A3. HCN data products of the ALMA observations of HE1108-2813 with the moment map 0 (top left), moment 1 map (top middle) and moment 2 map (top right). The position velocity diagram is on the bottom left and the spectra is on the bottom right.

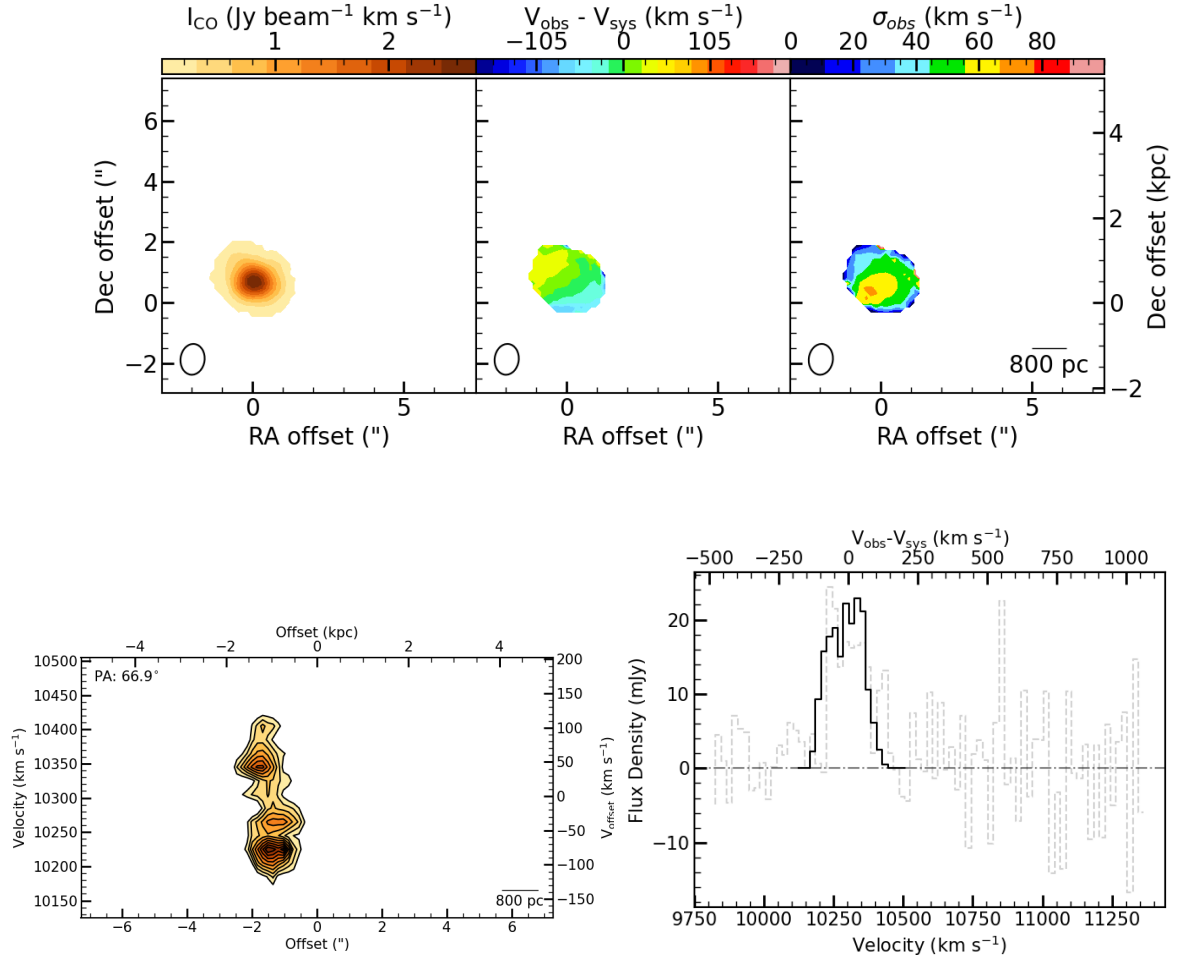


Figure A4. HCO+ data products of the ALMA observations of HE0433-1028 with the moment map 0 (top left), moment 1 map (top middle) and moment 2 map (top right). The position velocity diagram is on the bottom left and the spectra is on the bottom right.

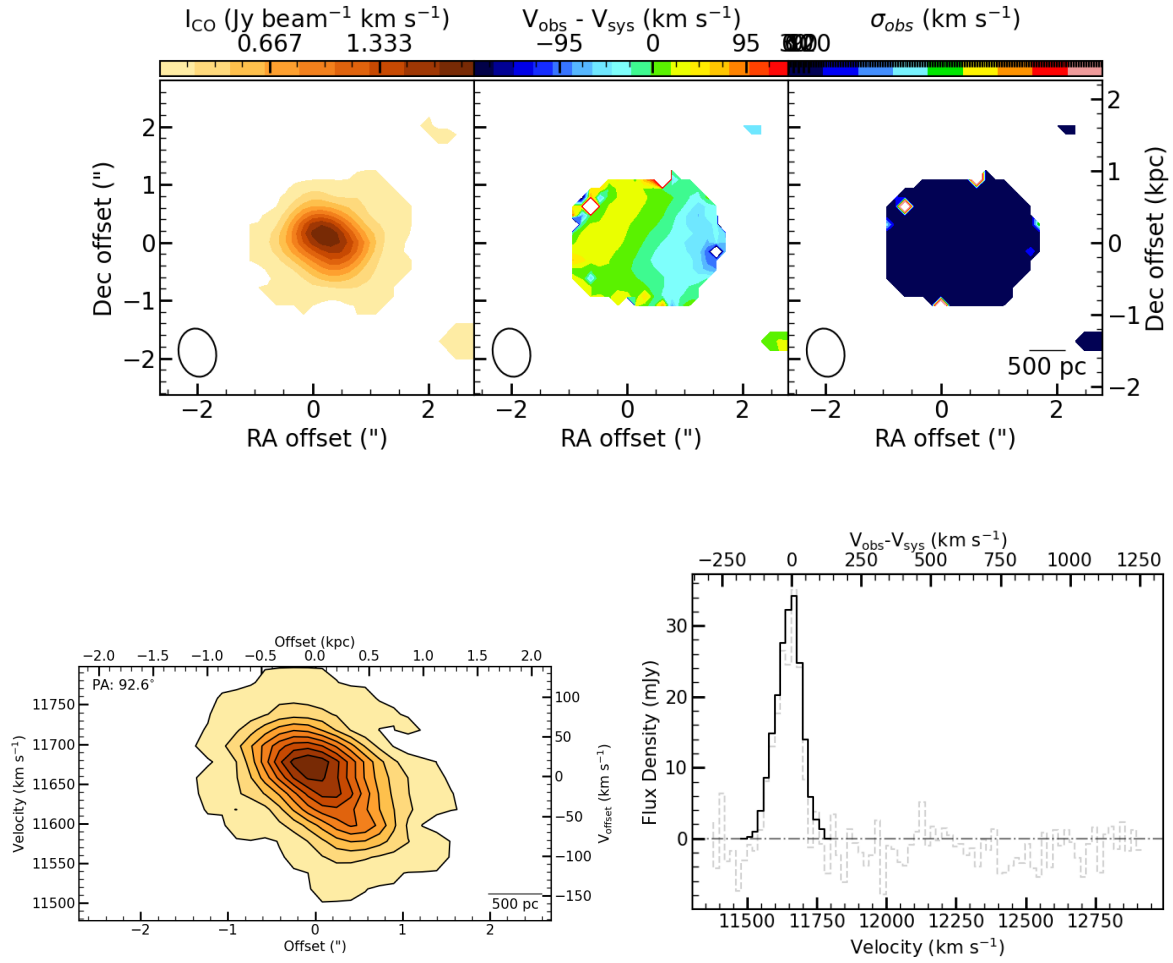


Figure A5. HCO+ data products of the ALMA observations of HE1029-1831 with the moment map 0 (top left), moment 1 map (top middle) and moment 2 map (top right). The position velocity diagram is on the bottom left and the spectra is on the bottom right.

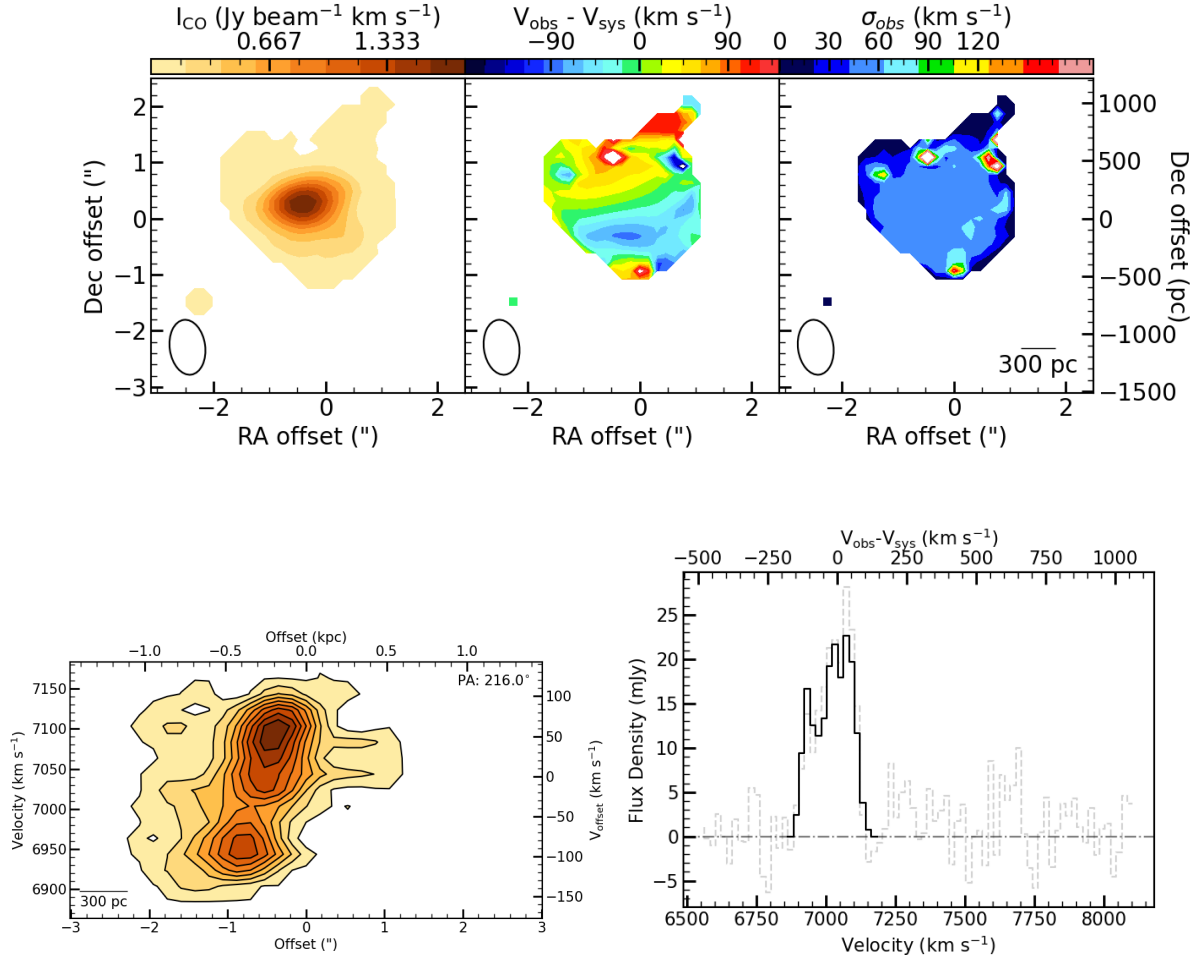


Figure A6. CO data products of the ALMA observations of HE1108-2813 with the moment map 0 (top left), moment 1 map (top middle) and moment 2 map (top right). The position velocity diagram is on the bottom left and the spectra is on the bottom right.

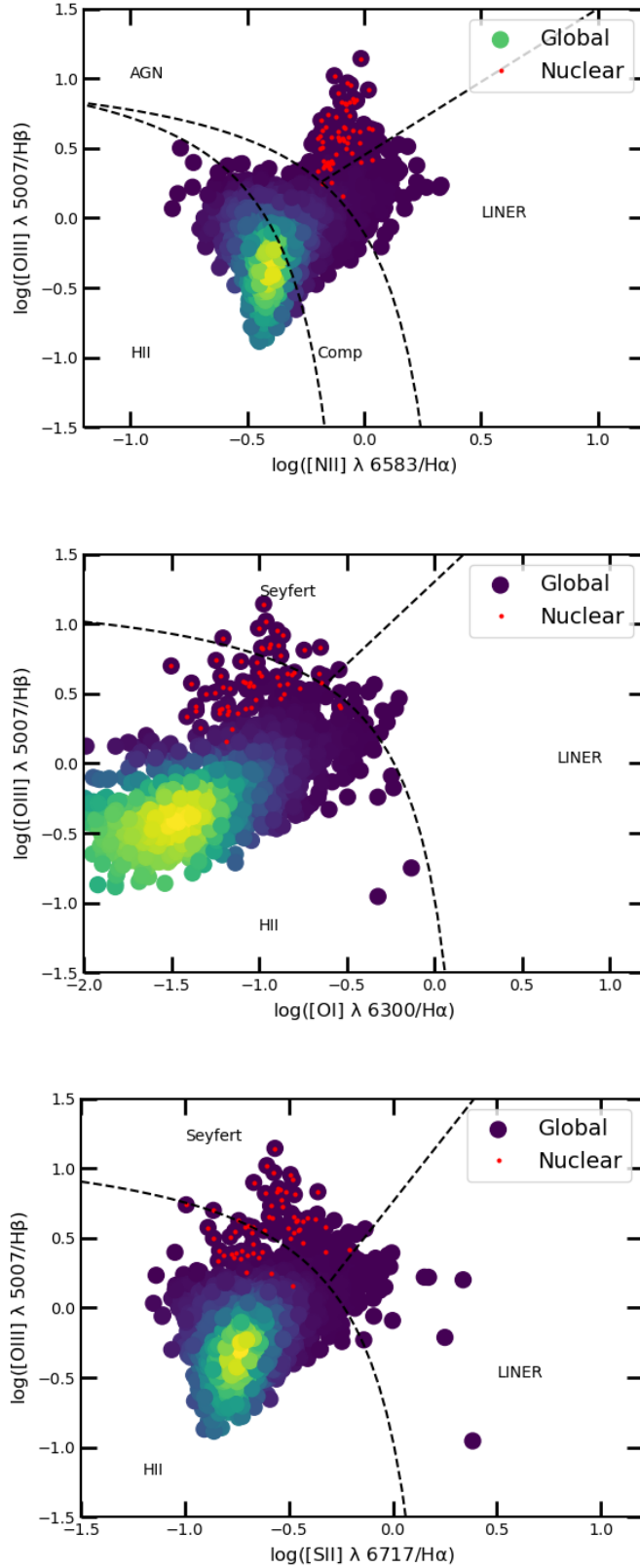


Figure A7. Global optical AGN classifications for HE0433-1028 with the BPT diagram at the top, the VO87-OI diagram in the middle and the VO87-SII diagram at the bottom. The red points represent the nuclear region taken within one ALMA beam size.

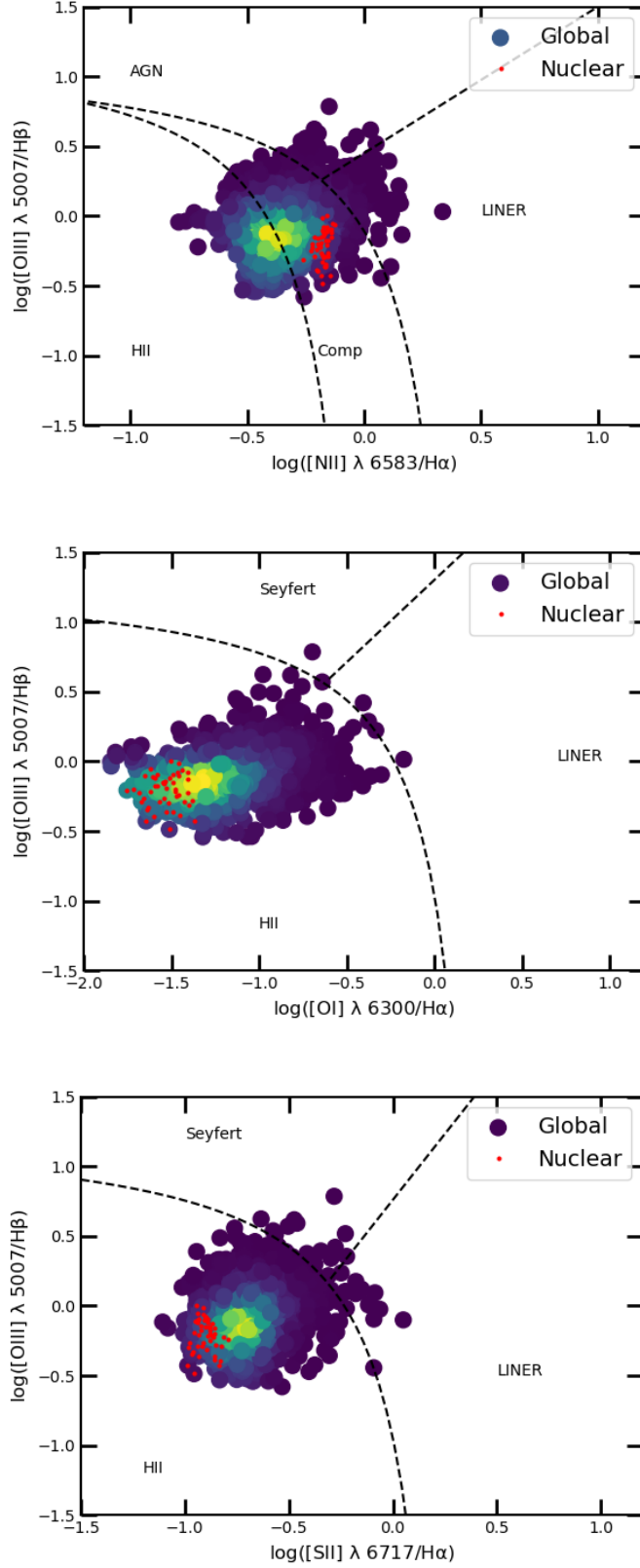


Figure A8. Global optical AGN classifications for HE1029-1831 with the BPT diagram at the top, the VO87-OI diagram in the middle and the VO87-SII diagram at the bottom. The red points represent the nuclear region taken within one ALMA beam size.

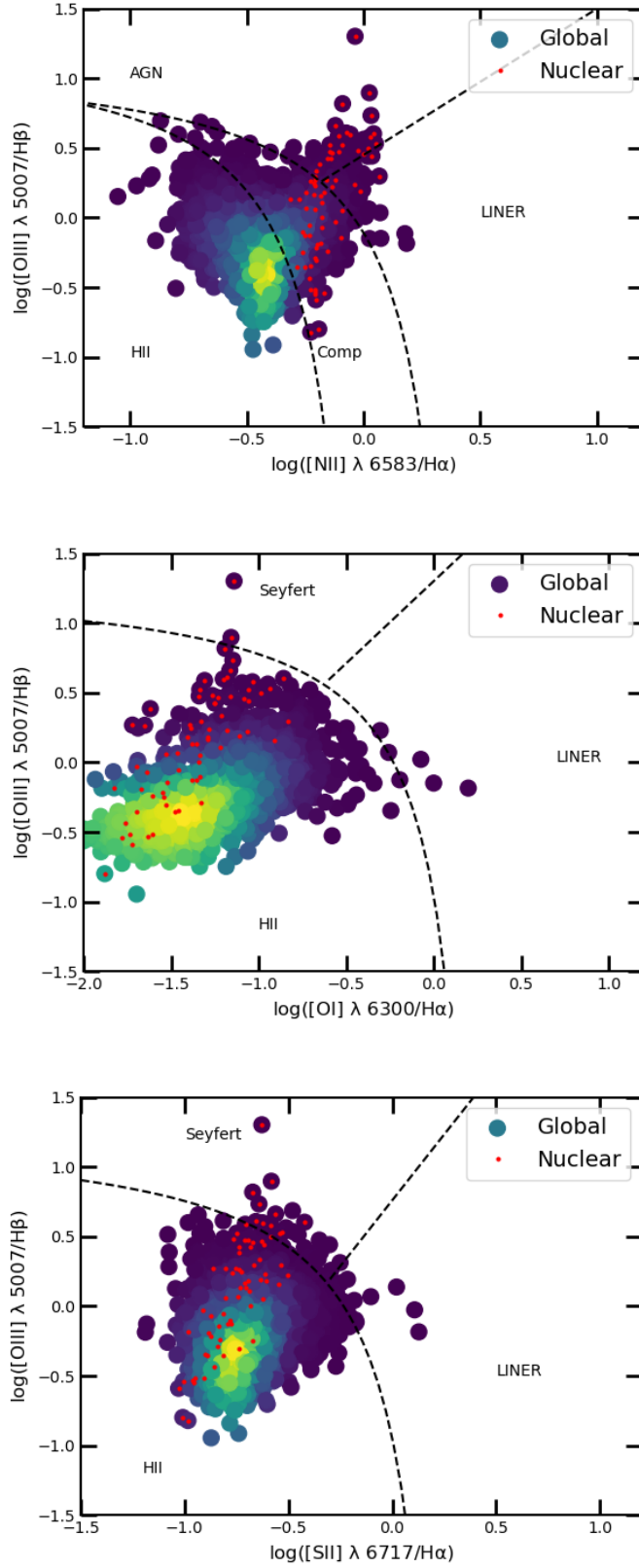


Figure A9. Global optical AGN classifications for HE1108-2813 with the BPT diagram at the top, the VO87-OI diagram in the middle and the VO87-SII diagram at the bottom. The red points represent the nuclear region taken within one ALMA beam size.

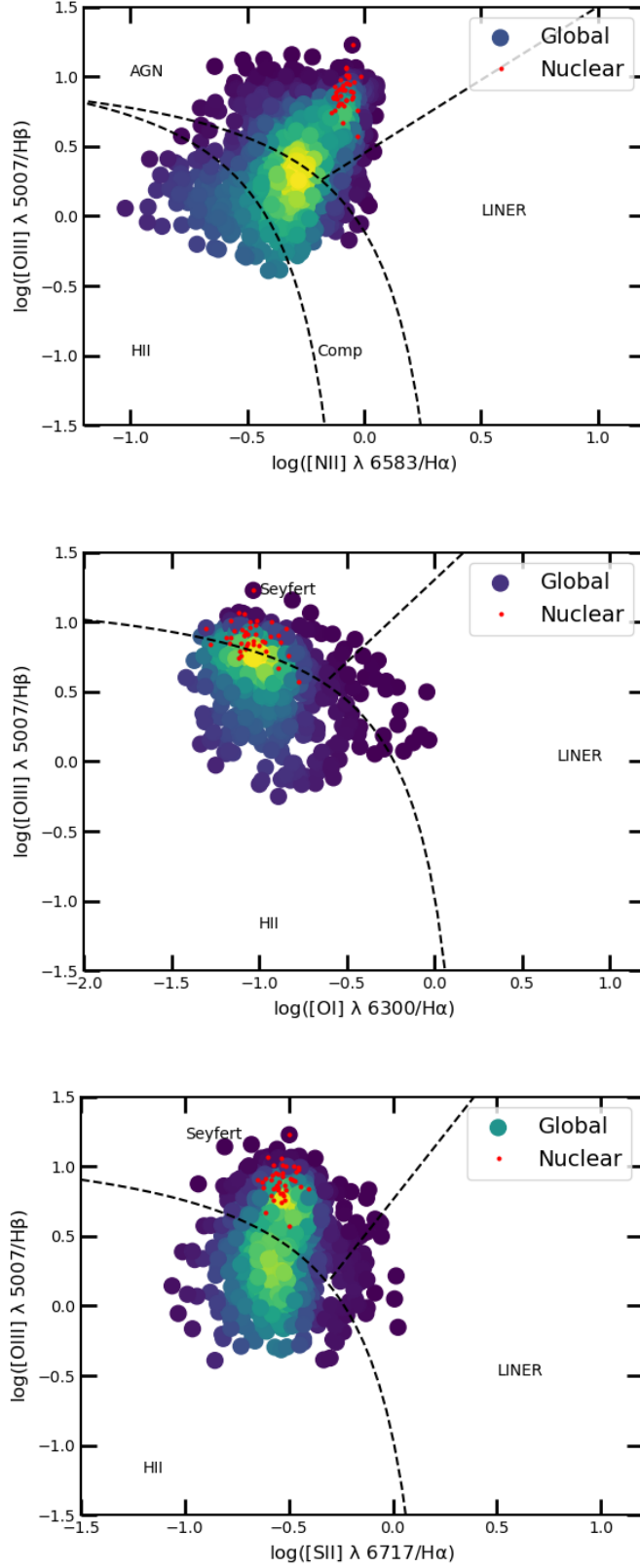


Figure A10. Global optical AGN classifications for HE1353-1917 with the BPT diagram at the top, the VO87-OI diagram in the middle and the VO87-SII diagram at the bottom. The red points represent the nuclear region taken within one ALMA beam size.